Green Chemistry

PAPER

Biomass-derived porous carbon materials with sulfur and nitrogen dual-doping for energy storage†

Guiyin Xu, Jinpeng Han, Bing Ding, Ping Nie, Jin Pan, Hui Dou, Hongsen Li and Xiaogang Zhang*

Nowadays, energy shortage is a serious socioeconomic problem. The recovery of biomass can make a very significant contribution in alleviating the burden on already-strained energy resources. Broad beans, which are abundant in amino acids and vitamins, are extensively cultivated worldwide. However, a large quantity of by-product, broad bean shells, remains unused and pollutes the environment from the incinerating and/or uncontrolled decomposition that results. In this paper, we report the synthesis of sulfur and nitrogen dual-doping porous carbon materials, for use as the electrode materials of energy storage devices, produced by carbonizing the shells of broad beans by a chemical activation. The specific capacitance of the as-prepared porous carbon material is as high as 202 F g^{-1}, with a superior cycling performance for electric double layer capacitors at a current density of 0.5 A g^{-1}. Furthermore, it also shows a stable performance for lithium ion batteries and sodium ion batteries, which suggests that it has a promising potential for wide applications in the field of energy storage devices.

Introduction

Biomass is an available natural resource.[1,2] If it is allowed to incinerate, it will contribute to the greenhouse effect, fog and other detrimental environmental effects. Therefore, the conversion of biomass is becoming a hot research topic worldwide. Broad beans are a crop widely used as a human foodstuff. However, tons of broad beans shells (SBs), the by-product of broad beans, are produced every year. Although SBs are traditionally fed to animals, there are still a large quantity to be incinerated or abandoned. As a legume, SBs are rich in amino acids and vitamins.[3] Therefore, SBs can be transformed into carbon materials with heteroatom doping by calcining them in an inert gas (Fig. 1), which offers significant environmental benefits. Heteroatom-doped carbon materials have a wide range of applications, such as catalysis,[4,5] biosensing,[6] bioimaging,[7] energy conversion,[8,9] energy storage systems,[10–12] and other electronic devices.[13,14] Among the current energy storage options, electric double layer capacitors (EDLCs), lithium ion batteries (LIBs), and sodium ion batteries (SIBs)
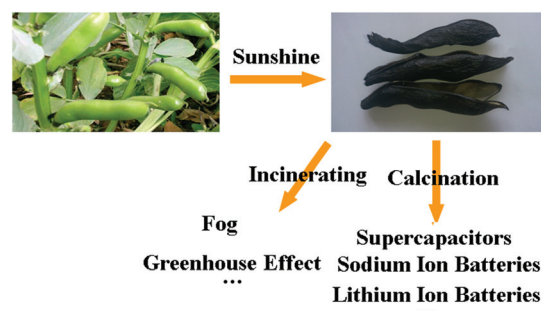
Jiangsu Key Laboratory of Materials and Technology for Energy Conversion, College of Material Science and Engineering, Nanjing University of Aeronautics and Astronautics, Nanjing, 210016, P. R. China. E-mail: azhangxg@163.com; Fax: +86-025-52112626; Tel: +86-025-52112626

Fig. 1 Illustration for the different processing methods of SBs.

receive considerable attention because of their high power and energy density.[15–20]

In recent years, porous carbon materials have been found to be promising candidates for EDLCs and LIBs because of their high electrical conductivity, large specific area, and easy availability.[21–23] There have been many reports about porous carbon materials, for example, mesoporous carbon spheres,[24] reduced graphene oxide (GO),[25,26] and carbide-derived carbon thin film[27] as electrodes for EDLCs and carbon nanotube graphene,[28] hollow carbon capsules,[29] and hollow carbon nanospheres[30] as anodes for LIBs. In the past, a lot of porous carbon materials were prepared by soft or hard template synthesis methods,[16,17,31–33] in which the synthesis process was complex and the yield was often low. Furthermore, the optim-

ization of porous carbon materials by further modification is well adapted for practical applications.[12,34] Porous carbon materials with sulfur or nitrogen doping can enhance the specific capacitance for EDLCs[35,36] and improve the specific capacity or rate capability for LIBs/SIBs.[8,37–39]

Combined with the increasing environmental problems caused by incinerating SBs, a method is proposed of employing the waste by-product to prepare porous carbon materials for energy storage applications. In this paper, porous carbon materials with heteroatom doping are presented for use as energy storage devices obtained by carbonization of the shells of broad beans (CSB) in an inert gas and then further chemical activation (ACSB). Compared to the previous methods of synthesizing porous heteroatom doped carbon materials, this work has several advantages: (1) SBs are resource-rich and sustainable and this results in a low cost; (2) SBs are abundant in nitrogen and sulfur and thus they are an ideal precursor for sulfur and nitrogen dual-doping carbon materials; (3) the overall synthesis process is simple and easy to handle, which makes it suitable for industrial production; and (4) the obtained porous carbon material (ACSB) has a large specific surface area, unique pore size distribution, sulfur–nitrogen dual-doping, and high electrical conductivity which could be widely applied in energy storage devices. Simultaneously, the electrochemical results demonstrate that the as-prepared carbon materials are promising candidates for energy storage devices.

Results and discussion

In the search for renewable resources for the sustainable development of low-cost energy storage devices, SBs are an abundant and attractive biomaterial (Fig. 2a) which has aroused much interest. More importantly, SBs are rich in protein, which is mainly composed of carbon, hydrogen, oxygen, nitrogen, and sulfur. Therefore, SBs are a promising precursor for synthesizing carbon materials with heteroatom doping. Interestingly, the morphology of SBs is like graphene, as shown in Fig. 2b, and displays a wrinkled laminar structure similar to the previous reports of graphene.[25,40] The transmission electron microscopy (TEM) image demonstrates the laminar structure of SBs (Fig. 2c). Meanwhile, thermal gravimetric (TG) analysis was carried out to investigate the carbonization process of SBs in an inert atmosphere. The TG curve shows a distinct weight loss stage from around 200 to 600 °C (Fig. 2d). The weight loss is primarily because of the evaporation of H_2O, CO_2 and CO, resulting from the escape of H and O atoms in SBs and leaving porous tunnels in CSB. The yield of the obtained material is as much as 25%. The industrial process for producing carbon-based materials is simple and the original material is low cost. Therefore, it is found to be suitable for industrial production (the inset of Fig. 3a).

Scanning electron microscopy (SEM) and TEM were also employed to investigate the structure of CSB and ACSB. Notably, there is no obvious change in the morphology after the carbonization of SBs (Fig. 3a, ESI Fig. S1†), which still shows the wrinkled structure. The TEM image further demonstrates the plate-like structure of CSB (Fig. 3d), confirming that the laminar structure still remains. Although CSB may exhibit some pores because of the pyrolysis of SBs and the evaporation of H_2O, CO_2 and CO during the carbonization process, the pores are not obvious in the typical SEM or TEM images.

As is well known, a high specific surface area benefits the rapid electronic and ionic transport for EDLCs and a large pore volume allows sufficient infiltration of the electrolyte and fast diffusion of lithium ion for LIBs.[41] Therefore, the specific surface area is enhanced in the next step. The chemical activation of carbon materials using potassium hydroxide (KOH) has received much attention.[42–44] The process for obtaining porous carbon materials is simple, controllable and does not consume expensive reagents. In this work, CSB is heated with KOH at 650 °C for 1 h under nitrogen to obtain ACSB. KOH can be completely transformed to potassium carbonate (K_2CO_3) at about 600 °C. And K_2CO_3 begins to decompose into CO_2 and potassium oxide at temperatures higher than 700 °C.
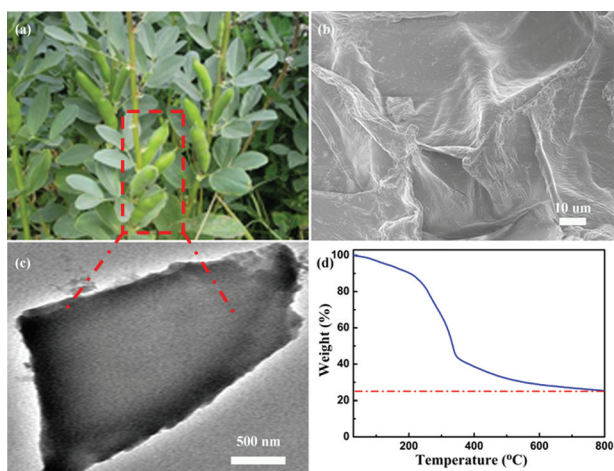

Fig. 2 (a) Digital photograph, (b) SEM image, and (c) TEM image of SBs. (d) TG curve of CSB from the pyrolysis of SBs under an inert atmosphere.
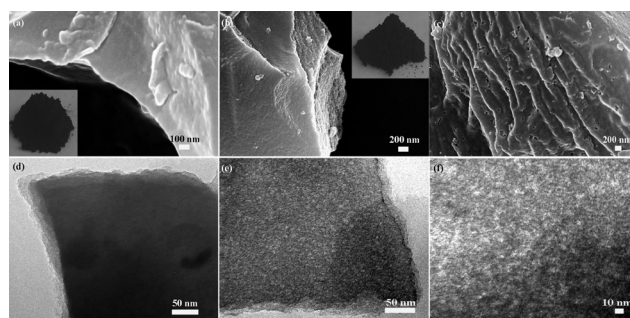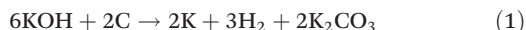

Fig. 3 (a) SEM image (the inset is a digital photograph of CSB) and (d) TEM image of CSB. (b) SEM image (the inset is a digital photograph of ACSB) and (e) TEM image of ACSB at the edge. (c) SEM image and (f) TEM image of ACSB in the middle.

Therefore, the optimum reaction equation between CSB and KOH is:[45]

$$6KOH + 2C \rightarrow 2K + 3H_2 + 2K_2CO_3 \qquad (1)$$

The yield of ACSB is approximately 71.3%, which is higher than the carbon yields of approximately 36% and 50% reported in previous papers.[46,47] After the activation, SEM images of ACSB indicate that the laminar structure (Fig. 3b) and the wrinkled structure (Fig. 3c) still remain. Simultaneously, there are abundant pores on the surface of ACSB (Fig. 3c), confirming that KOH can effectively create plentiful pores in carbon materials. The TEM images demonstrate the existence of the plate-like structure and rich pores in ACSB (Fig. 3e, f), which corresponds with the SEM observation. The high resolution transmission electron microscopy (HRTEM) image further reveals the structure of ACSB, which consists of tiny graphite domains (ESI Fig. S2a†).[48] Also, the abundant worm-like micropores and mesopores can be clearly observed in Fig. S2b (ESI†). The unique pore size distribution of ACSB could enable fast ion transport and allow sufficient infiltration of the electrolyte for EDLCs and LIBs/SIBs.

SBs contains essential amino acids and vitamins, which are abundant in nitrogen. Therefore, X-ray photoelectron spectroscopy (XPS) was carried out to detect the differences in the nitrogen bonds in CSB and ACSB. The nitrogen peaks of ACSB could be fitted into four peaks (Fig. 4a).[8,21] The first peak at

403.3 eV corresponds to the *N*-oxides of pyridine-N (**N1**). The second peak at 401.0 eV is identified as the quaternary-N (**N2**), which is the most stable nitrogen species in the carbonization process of SBs and the activation process of CSB. The third peak at 399.9 eV can be attributed to pyrrolic-N (**N3**). The last peak located at 398.5 eV is attributed to the hexagonal pyridinic-N (**N4**). Interestingly, thiamine (Fig. 4b, c) and some sulfur-containing amino acids are also present in the composition of SBs,[49] which results in ACSB being doped with sulfur. The sulfur peaks of ACSB could be fitted into three peaks (Fig. 4d).[37,50,51] The first peak at 168.5 eV should be assigned to the oxidized sulfur species (**S1**), such as the sulfate (–C–SO$_4$–C–) or sulfonate (–C–SO$_3$–C–). The other two peaks at 165.2 and 164.0 eV correspond to the S2p$_{1/2}$ (**S2**) and S2p$_{3/2}$ (**S3**) of the –C–S–C– covalent bond, respectively. The presence of nitrogen and sulfur in CSB is similar to ACSB (ESI Fig. S3†). Only carbon, nitrogen, oxygen and sulfur are detected from CSB and ACSB within the range of XPS sensitivity (ESI Table S1†), indicating the existence of other impurities. The amounts of nitrogen and sulfur were 2.2% and 0.97% in CSB and 2.0% and 0.94% in ACSB, respectively. Combined with the XPS spectra and the results from a previous report,[12] the possible schematic illustration for the chemical structure of ACSB with nitrogen and sulfur dual-doping is shown in Fig. 4e. Furthermore, the elemental mapping images (Fig. 4f) demonstrate the uniform distribution of carbon, nitrogen, oxygen and sulfur in ACSB.

In the XRD patterns of CSB and ACSB, there are two broad signals around 24° and 44° (Fig. 5a), which correspond to the (002) and (100) spacing of the graphene stacks, respectively.[52] XRD results indicate that these carbon materials have no impurities, corroborating well with the XPS observation. The presence of trace metals in SBs,[49] such as iron, may favor the improvement of the degree of graphitization for CSB and ACSB. The diffraction intensity of the (002) and (100) peak in ACSB is lower than those in CSB under the same conditions of detection, resulting from the chemical activation by KOH to
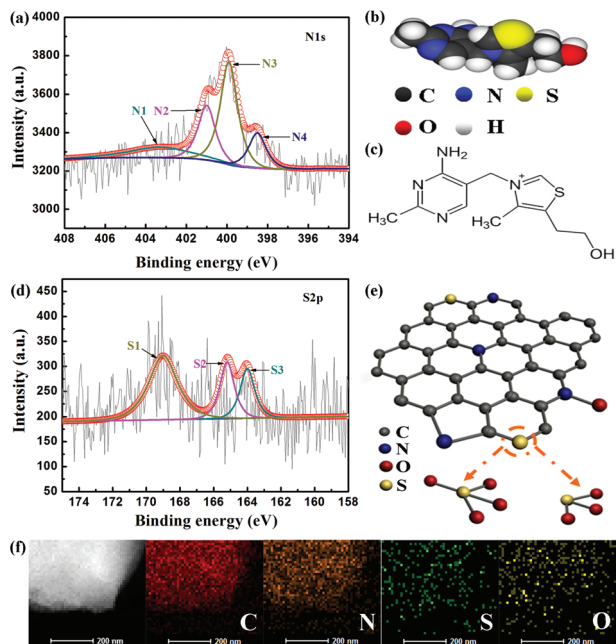

Fig. 4 (a) N1s XPS spectra for ACSB (N1: *N*-oxides of pyridine-N; N2: quaternary-N; N3: pyrrolic-N; N4: pyridinic-N). (b) The structural model and (c) structural formula of thiamine. (d) S2p XPS spectra for ACSB (S1: the oxidised sulfur species; S2: the S2p$_{1/2}$ of –C–S–C–; S3: the S2p$_{3/2}$ of –C–S–C–) and (e) a schematic illustration for the chemical structure of ACSB with nitrogen and sulfur dual-doping. (f) STEM image of ACSB and the corresponding elemental mapping images for carbon, nitrogen, sulfur and oxygen.
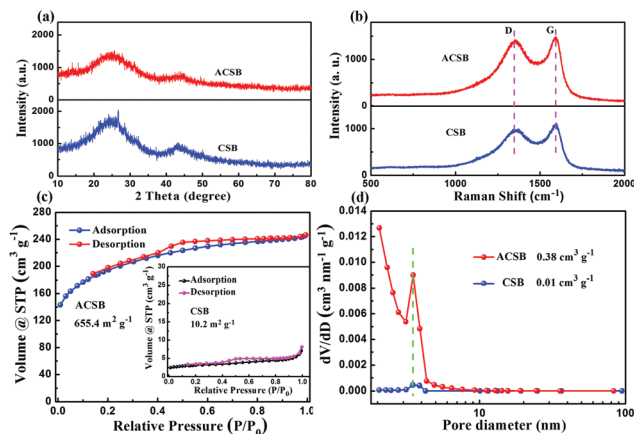

Fig. 5 (a) XRD patterns. (b) Raman spectra. (c) N$_2$ adsorption–desorption isotherms at 77 K and (d) PSD curves of CSB and ACSB. PSD is calculated using the Barrett–Joyner–Halenda (BJH) method.

break down the hexagonal symmetry of the graphite lattice and lead to lattice defects in ACSB. The structures of the as-prepared carbon materials were further detected using Raman spectra. Two strong bands located at around 1355 and 1590 cm^{-1} were assigned to the D-band (D) and the G-band (G),[53] respectively (Fig. 5b). D could originate from the disorder-induced features of carbon and structural defects, because of the nitrogen, sulfur and oxygen heteroatom doping in the carbon materials and the chemical activation in ACSB. The increased intensity of D in ACSB also indicates the generation of defects after the chemical activation. Furthermore, it could be calculated that the relative intensity ratio of D and G (ID/IG) increases from 0.88 (CSB) to 0.96 (ACSB), showing that the degree of graphitization of ACSB decreases; while G corresponds to the sp^2 carbon-bonded graphitic structure, which is beneficial for enhancing the electrical conductivity of carbon materials.[54] Furthermore, the appearance of G indicates the presence of graphitic domains,[55] which are consistent with the HRTEM observation. The carbon materials obtained would favor the improvement of electrical conductivity when used as electrode materials for energy storage devices.

N$_2$ adsorption/desorption isotherms and the corresponding pore size distribution (PSD) curves for CSB and ACSB were acquired (Fig. 5c, d). The specific surface area and PSD were calculated using the Brunauer–Emmett–Teller (BET) method and Barrett–Joyner–Halenda (BJH) method. The isotherms of ACSB are typical type I and type IV isotherms with a hysteresis loop, indicating the presence of micropores and mesopores.[56] In detail, the isotherms have a clear upwards trend at the low relative pressure ($P/P_0 < 0.4$), showing that ACSB is rich in micropores. The appearance of significant hysteresis characteristics at high relative pressure ($P/P_0 = 0.4$–0.8) in the isotherms demonstrates the existence of abundant mesopores. Therefore, ACSB exhibits a highly developed hierarchical porosity network of micropores in combination with mesopores, while the isotherms of CSB are typical type IV isotherms with a hysteresis loop (the inset of Fig. 5c), indicating the presence of mesopores. Meanwhile, a slight upward tendency at the high relative pressure ($P/P_0 = 0.95$–1.0) corresponds to the presence of macropores, resulting from the accumulation of carbon particles. The PSD data indicates the size of the majority of pores is about 3 nm in CSB and ACSB. A clear upward trend peak (<2 nm) further confirms the abundant micropores in ACSB. The chemical activation effectively creates abundant pores, resulting in a specific surface area ranging from 10.2 to 655.4 m^2 g^{-1} and a total pore volume ranging from 0.01 to 0.38 cm^3 g^{-1} (Table S4†).

Cyclic voltammetry (CV) and galvanostatic charge/discharge measurements in a three-electrode system were carried out to investigate the electrochemical performance of CSB and ACSB as electrode materials for EDLCs. The regular rectangular shapes are present at low scan rates, which is the typical characteristic of EDLCs. The approximately rectangular shape of the CV curve can still be maintained even when the scan rate is as high as 100 mV s^{-1} (Fig. 6a), indicating that rapid ion transport can be operated in ACSB. The galvanostatic
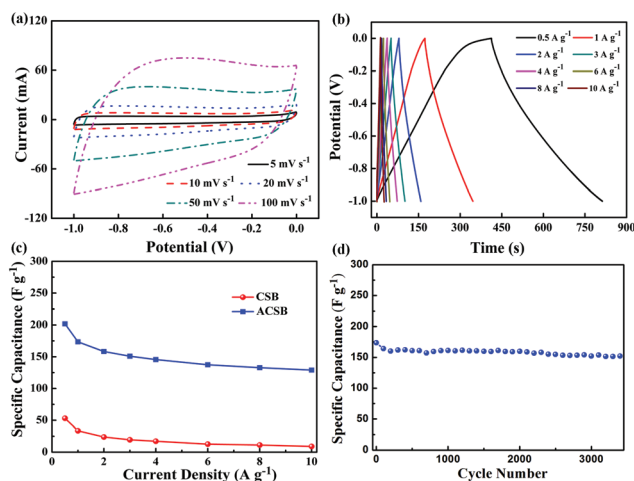

Fig. 6 (a) CV curves of the ACSB electrode in 6 M KOH aqueous solution at different scan rates. (b) The galvanostatic charge–discharge curves of the ACSB electrode at different current densities. (c) The specific capacitances calculated from the discharge curves under different current densities. (d) Cyclic stability of the ACSB-based EDLCs at a current density of 1 A g^{-1}.

charge/discharge curves of the ACSB electrode at different current densities show almost isosceles triangular shapes (Fig. 6b), demonstrating the ideal charge and discharge characteristics for EDLCs. Although CSB has a low specific surface area, the sulfur and nitrogen doping could increase the specific capacitance (ESI Fig. S4†). The incorporation of sulfur in carbon materials can increase the space utilization by a specific electrosorption of electrolyte ions and contribute to pseudocapacitance.[35] The incorporation of nitrogen in carbon materials can increase the electrical conductivity, wettability, and contribute to a pseudocapacitive effect.[44] CSB has specific capacitances of 53 F g^{-1} at a current density of 0.5 A g^{-1} and 34 F g^{-1} at 1 A g^{-1} (ESI Table S5†), which is marginally higher than the previous reports of 100% carbon nanotube (CNT) film (24 F g^{-1}) and pristine CNT paper (32 F g^{-1}).[57,58] After the KOH activation, the hierarchically porous structure in ACSB could favor fast electron and ion transport (ESI Fig. S5†). Therefore, ACSB exhibits a high specific capacitance of 202 F g^{-1} at 0.5 A g^{-1}. Even at a current density of 10 A g^{-1}, the specific capacitance is still as much as 129 F g^{-1}, which is higher than the results of previous reports (ESI Table S6†). Furthermore, ACSB exhibits a superior rate performance, as shown in Fig. 6c. Simultaneously, the retention of specific capacitance for the ACSB electrode is close to 90% after 3000 cycles (Fig. 6d), showing it presents an excellent cycling stability. In addition, ACSB delivers a high specific capacitance of 229 F g^{-1} at a current density of 0.5 A g^{-1} in 1 M H$_2$SO$_4$ (Fig. S6†), which is higher than the specific capacitances of GO/CNT hybrid powder (180 F g^{-1} at 0.4 A g^{-1}) and 66.7 wt% CNTs (approximately 180 F g^{-1} at 0.5 A g^{-1}) in previous reports.[57,59]

Inspired by the commercialization of graphite as an anode for LIBs, CR2032-type coin cells were assembled to estimate
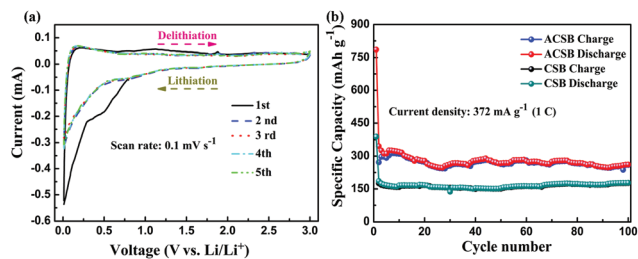
Fig. 7 (a) Typical CV curves of the ACSB anode for LIBs at a scan rate of 0.1 mV s⁻¹. (b) Cycling performance of the CSB and ACSB anodes for LIBs at a constant rate of 1 C (1 C = 372 mA g⁻¹).

the electrochemical performance of CSB and ACSB electrodes. There is no obvious change after the first cycle in the CV curves of the ACSB electrode (Fig. 7a), which display a superior reactive reversibility and cycling stability for LIBs. The initial discharge capacities of CSB and ACSB are 467.1 and 845.2 mA h g⁻¹, respectively, at a current rate of 0.5 C (ESI Fig. S7†). Simultaneously, the two anode materials reveal good cycling performance after the first cycle, which agrees well with the CV curves. Even at a current rate of 1 C, the discharge capacity of CSB is still 178.1 mA h g⁻¹ and the discharge capacity of ACSB is as much as 261.5 mA h g⁻¹ after 100 cycles (Fig. 7b), which are superior to the values for three-dimensional multiwall CNTs-graphene-polyethylene terephthalate (~100 mA h g⁻¹ at 316 mA g⁻¹)[28] and graphite (~150 mA h g⁻¹ at 300 mA g⁻¹).[29] The favorable electrochemical performance of the CSB anode could be attributed to the dual-doping of sulfur and nitrogen. The further improvement of the electrochemical performance for the ACSB anode is benefited from the hierarchically porous structure and the dual-doping of sulfur and nitrogen. The porous structure of ACSB could allow sufficient infiltration of the electrolyte and shorten the transport pathway for both electrons and ions (ESI Fig. S8†).

Recently, SIBs have received worldwide attention because of their abundant storage capacity and low cost of sodium.[60–62] When the ACSB electrode was tested as the anode material for SIBs, the initial discharge capacity is 466.3 mA h g⁻¹ at a current density of 200 mA g⁻¹ (Fig. 8a). The irreversible capacity loss occurring during the first cycle results from the electrolyte decomposition to form a solid-electrolyte interphase (SEI) layer on the surface of the electrodes.[63] The galvanostatic charge/discharge profiles of the ACSB electrode are similar to those found in previous reports, representing
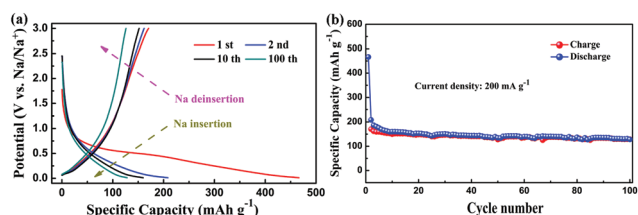
the insertion/deinsertion of sodium in ACSB.[39,64] As shown in Fig. 8b, the ACSB electrode shows outstanding cycling performance, which is superior to that of AG and carbon nanofibre electrodes,[39,48] demonstrating that the as-prepared materials have great potential in the applications of SIBs.

Conclusions

In summary, sulfur and nitrogen dual-doped porous carbon materials have been successfully prepared from the shells of broad beans and applied to the production of EDLCs, LIBs and SIBs. The specific capacitance is as much as 129 F g⁻¹ for EDLCs at a high current density of 10 A g⁻¹; the discharge capacity at a current rate of 1 C still remains at 261.5 mA h g⁻¹ for LIBs after 100 cycles; and the initial discharge capacity is as high as 466.3 mA h g⁻¹ for SIBs at a current density of 200 mA g⁻¹. These electrochemical results clearly prove ACSB to be a promising candidate for energy storage applications. Based on this research, the activating agent species (water vapor, zinc chloride, and phosphoric acid) and weight ratio of activating agents to carbon precursors should be specially tailored to obtain the optimal porous carbon materials for different energy storage devices, such as lithium-air batteries, lithium-sulfur batteries and photocatalysis.

Acknowledgements

Notes and references

1 N. Liu, K. Huo, M. T. McDowell, J. Zhao and Y. Cui, *Sci. Rep.*, 2013, **3**, 1919.
2 L. Y. Zhang, Y. Y. Wang, B. Peng, W. T. Yu, H. Y. Wang, T. Wang, B. W. Deng, L. Y. Chai, K. Zhang and J. X. Wang, *Green Chem.*, 2014, **16**, 3926–3934.
3 X. Wang, G. Liu, Q. Ou, X. Zhao, J. Hao and X. Zhou, *Asian J Agric. Res.*, 2013, **5**, 111–113.
4 M. Zhong, E. K. Kim, J. P. McGann, S. E. Chun, J. F. Whitacre, M. Jaroniec, K. Matyjaszewski and T. Kowalewski, *J. Am. Chem. Soc.*, 2012, **134**, 14846–14857.
5 S. Yang, L. Zhi, K. Tang, X. Feng, J. Maier and K. Müllen, *Adv. Funct. Mater.*, 2012, **22**, 3634–3640.
6 Y. Wang, Y. Shao, D. W. Matson, J. Li and Y. Lin, *ACS Nano*, 2010, **4**, 1790–1798.

Fig. 8 (a) Galvanostatic charge/discharge profiles and (b) cycling performance of the ACSB anode for SIBs at a current density of 200 mA g⁻¹.

7 Y. Dong, H. Pang, H. B. Yang, C. Guo, J. Shao, Y. Chi, C. M. Li and T. Yu, *Angew. Chem., Int. Ed.*, 2013, **52**, 7800–7804.

8 L. Qie, W. M. Chen, Z. H. Wang, Q. G. Shao, X. Li, L. X. Yuan, X. L. Hu, W. X. Zhang and Y. H. Huang, *Adv. Mater.*, 2012, **24**, 2047–2050.

9 J. P. Paraknowitsch and A. Thomas, *Energy Environ. Sci.*, 2013, **6**, 2839–2855.

10 L. F. Chen, Z. H. Huang, H. W. Liang, Q. F. Guan and S. H. Yu, *Adv. Mater.*, 2013, **25**, 4746–4752.

11 L. F. Chen, X. D. Zhang, H. W. Liang, M. Kong, Q. F. Guan, P. Chen, Z. Y. Wu and S. H. Yu, *ACS Nano*, 2012, **6**, 7092–7102.

12 J. Liang, Y. Jiao, M. Jaroniec and S. Z. Qiao, *Angew. Chem., Int. Ed.*, 2012, **51**, 11496–11500.

13 P. Zhang, Y. Gong, H. Li, Z. Chen and Y. Wang, *Nat. Commun.*, 2013, **4**, 1593.

14 P. G. Bruce, S. A. Freunberger, L. J. Hardwick and J. M. Tarascon, *Nat. Mater.*, 2012, **11**, 19–29.

15 C. Merlet, B. Rotenberg, P. A. Madden, P. L. Taberna, P. Simon, Y. Gogotsi and M. Salanne, *Nat. Mater.*, 2012, **11**, 306–310.

16 H. Jiang, P. S. Lee and C. Li, *Energy Environ. Sci.*, 2013, **6**, 41–53.

17 Y. Li, Z. Y. Fu and B. L. Su, *Adv. Funct. Mater.*, 2012, **22**, 4634–4667.

18 L. Yin, J. Wang, F. Lin, J. Yang and Y. Nuli, *Energy Environ. Sci.*, 2012, **5**, 6966–6972.

19 D. R. MacFarlane, N. Tachikawa, M. Forsyth, J. M. Pringle, P. C. Howlett, G. D. Elliott, J. H. Davis, M. Watanabe, P. Simon and C. A. Angell, *Energy Environ. Sci.*, 2014, **7**, 232–250.

20 D. W. Su, S. X. Dou and G. X. Wang, *J. Mater. Chem. A*, 2014, **2**, 11185–11194.

21 G. Xu, B. Ding, P. Nie, L. Shen, J. Wang and X. Zhang, *Chem. – Eur. J.*, 2013, **19**, 12306–12312.

22 S. Wang, R. Liu, C. Han, J. Wang, M. Li, J. Yao, H. Li and Y. Wang, *Nanoscale*, 2014, **6**, 13510–13517.

23 Y. Gong, Z. Wei, J. Wang, P. Zhang, H. Li and Y. Wang, *Sci. Rep.*, 2014, **4**, 6349.

24 Q. Li, R. Jiang, Y. Dou, Z. Wu, T. Huang, D. Feng, J. Yang, A. Yu and D. Zhao, *Carbon*, 2011, **49**, 1248–1257.

25 Y. Yoon, K. Lee, C. Baik, H. Yoo, M. Min, Y. Park, S. M. Lee and H. Lee, *Adv. Mater.*, 2013, **25**, 4437–4444.

26 J. H. Lee, N. Park, B. G. Kim, D. S. Jung, K. Im, J. Hur and J. W. Choi, *ACS Nano*, 2013, **7**, 9366–9374.

27 T. M. Arruda, M. Heon, V. Presser, P. C. Hillesheim, S. Dai, Y. Gogotsi, S. V. Kalinin and N. Balke, *Energy Environ. Sci.*, 2013, **6**, 225–231.

28 C. Kang, R. Baskaran, J. Hwang, B. C. Ku and W. Choi, *Carbon*, 2014, **68**, 493–500.

29 M. S. Kim, B. Fang, J. H. Kim, D. Yang, Y. K. Kim, T. S. Bae and J. S. Yu, *J. Mater. Chem.*, 2011, **21**, 19362–19367.

30 K. Tang, R. J. White, X. Mu, M. M. Titirici, P. A. van Aken and J. Maier, *ChemSusChem*, 2012, **5**, 400–403.

31 W. Li and D. Zhao, *Chem. Commun.*, 2013, **49**, 943–946.

32 Y. Fang, D. Gu, Y. Zou, Z. Wu, F. Li, R. Che, Y. Deng, B. Tu and D. Zhao, *Angew. Chem., Int. Ed.*, 2010, **49**, 7987–7991.

33 Y. Wang and Y. Xia, *Adv. Mater.*, 2013, **25**, 5336–5342.

34 Z. Liu, H. Nie, Z. Yang, J. Zhang, Z. Jin, Y. Lu, Z. Xiao and S. Huang, *Nanoscale*, 2013, **5**, 3283–3288.

35 M. Seredych and T. J. Bandosz, *J. Mater. Chem. A*, 2013, **1**, 11717–11727.

36 L. Wei, M. Sevilla, A. B. Fuertes, R. Mokaya and G. Yushin, *Adv. Funct. Mater.*, 2012, **22**, 827–834.

37 Y. Yan, Y. X. Yin, S. Xin, Y. G. Guo and L. J. Wan, *Chem. Commun.*, 2012, **48**, 10663–10665.

38 Y. Mao, H. Duan, B. Xu, L. Zhang, Y. Hu, C. Zhao, Z. Wang, L. Chen and Y. Yang, *Energy Environ. Sci.*, 2012, **5**, 7950–7955.

39 H. G. Wang, Z. Wu, F. L. Meng, D. L. Ma, X. L. Huang, L. M. Wang and X. B. Zhang, *ChemSusChem*, 2013, **6**, 56–60.

40 N. W. Li, M. B. Zheng, H. L. Lu, Z. B. Hu, C. F. Shen, X. F. Chang, G. B. Ji, J. M. Cao and Y. Shi, *Chem. Commun.*, 2012, **48**, 4106–4108.

41 G. Xu, B. Ding, L. Shen, P. Nie, J. Han and X. Zhang, *J. Mater. Chem. A*, 2013, **1**, 4490–4496.

42 Y. Zhu, S. Murali, M. D. Stoller, K. J. Ganesh, W. Cai, P. J. Ferreira, A. Pirkle, R. M. Wallace, K. A. Cychosz, M. Thommes, D. Su, E. A. Stach and R. S. Ruoff, *Science*, 2011, **332**, 1537–1541.

43 L. Zhang, F. Zhang, X. Yang, G. Long, Y. Wu, T. Zhang, K. Leng, Y. Huang, Y. Ma, A. Yu and Y. Chen, *Sci. Rep.*, 2013, **3**, 1408.

44 J. Wei, D. Zhou, Z. Sun, Y. Deng, Y. Xia and D. Zhao, *Adv. Funct. Mater.*, 2013, **23**, 2322–2328.

45 J. Wang and S. Kaskel, *J. Mater. Chem.*, 2012, **22**, 23710–23725.

46 D. Huličová, K. Hosoi, S. I. Kuroda, H. Abe and A. Oya, *Adv. Mater.*, 2002, **14**, 452–455.

47 D. Hulicova, F. Sato, K. Okabe, M. Koishi and A. Oya, *Carbon*, 2001, **39**, 1438–1442.

48 W. Luo, J. Schardt, C. Bommier, B. Wang, J. Razink, J. Simonsen and X. Ji, *J. Mater. Chem. A*, 2013, **1**, 10662–10666.

49 Wikipedia, http://en.wikipedia.org/wiki/Vicia_faba#Other_uses, 2014.

50 F. Bottger-Hiller, A. Mehner, S. Anders, L. Kroll, G. Cox, F. Simon and S. Spange, *Chem. Commun.*, 2012, **48**, 10568–10570.

51 J. P. Paraknowitsch, A. Thomas and J. Schmidt, *Chem. Commun.*, 2011, **47**, 8283–8285.

52 G. Xu, B. Ding, P. Nie, L. Shen, H. Dou and X. Zhang, *ACS Appl. Mater. Interfaces*, 2013, **6**, 194–199.

53 X. Xu, Y. Li, Y. Gong, P. Zhang, H. Li and Y. Wang, *J. Am. Chem. Soc.*, 2012, **134**, 16987–16990.

54 K. Ai, Y. Liu, C. Ruan, L. Lu and G. Lu, *Adv. Mater.*, 2013, **25**, 998–1003.

55 R. Jia, J. Chen, J. Zhao, J. Zheng, C. Song, L. Li and Z. Zhu, *J. Mater. Chem.*, 2010, **20**, 10829–10834.

56 Y. S. Su and A. Manthiram, *Nat. Commun.*, 2012, **3**, 1166.

57 Z. D. Huang, B. Zhang, S. W. Oh, Q. B. Zheng, X. Y. Lin, N. Yousefi and J. K. Kim, *J. Mater. Chem.*, 2012, **22**, 3591–3599.

58 S. L. Chou, J. Z. Wang, S. Y. Chew, H. K. Liu and S. X. Dou, *ElectroChem. Commun.*, 2008, **10**, 1724–1727.

59 S. H. Aboutalebi, A. T. Chidembo, M. Salari, K. Konstantinov, D. Wexler, H. K. Liu and S. X. Dou, *Energy Environ. Sci.*, 2011, **4**, 1855–1865.

60 H. Zhu, Z. Jia, Y. Chen, N. Weadock, J. Wan, O. Vaaland, X. Han, T. Li and L. Hu, *Nano Lett.*, 2013, **13**, 3093–3100.

61 X. Yu, H. Pan, W. Wan, C. Ma, J. Bai, Q. Meng, S. N. Ehrlich, Y. S. Hu and X. Q. Yang, *Nano Lett.*, 2013, **13**, 4721–4727.

62 P. Nie, L. Shen, H. Luo, B. Ding, G. Xu, J. Wang and X. Zhang, *J. Mater. Chem. A*, 2014, **2**, 5852–5857.

63 K. T. Lee, R. Black, T. Yim, X. Ji and L. F. Nazar, *Adv. Energy Mater.*, 2012, **2**, 1490–1496.

64 S. Komaba, W. Murata, T. Ishikawa, N. Yabuuchi, T. Ozeki, T. Nakayama, A. Ogata, K. Gotoh and K. Fujiwara, *Adv. Funct. Mater.*, 2011, **21**, 3859–3867.